Origin of the Neoproterozoic Baijianshan banded iron formation at the southeastern margin of the Tarim Block in NW China: implication for an extremely reducing ocean

Xiao-Shu Hao   Chuan-Lin Zhang*   Hui-Chao Zhang   Teng Ding   Xian-Tao Ye

College of Oceanography, Hohai University, Nanjing 210098, P.R. China

Abstract: The Neoproterozoic Banded iron formations (BIFs) were closely associated with   during the breakup of the Rodinia, thus they played an important role   understanding of the atmospheric and oceanic oxygen levels during this period. In this contri   Neoproterozoic (ca. 737 Ma) Baijianshan BIF at Southeast Tarim, northwestern China w   Magnetite is the dominated iron-species, which occurs as the lamina interbedded with   contains low concentrations of trace elements, and is depleted in light rare earth   based on comparison with the Post Archean Australian Shale (PAAS). In additi   slightly positive La-Eu anomalies, negligible Ce anomalies, insignificant Y ano   ratios (23-32), and slightly chondritic initial   -0.4   All these features indicate that the precipitation of Baijianshan BIF   submarine low-T hydrothermal fluids with little detrital contribution. M

revealing the partial oxidation of Fe^{2+} into Fe^{3+} Our data suggest that the formation of Baijianshan BIF was   reducing ocean, which most likely was isolated from the oxid   Neoproterozoic Baijianshan ocean has the initial oxygen   Archean and Paleoproterozoic oceans.

Key words: Neoproterozoic, banded iron formations (BI

*Corresponding Author: E-Mail: zhangchuanlin@

1 Introduction

Banded iron formations (BIFs)   marine sedimentary rocks main   of sedimentary rock containi   thinly layered or laminate   that are composed mai   1983). The oldest B   formed during the   the references t   Ga) after a b   were close   Oxidati   oxyge   ba

Algoma-type   in the sequences mainly composed of
volcanic rocks, greywackes and turbi   Sh et al., 2015),
while the Superior-type were usually formed with sedimentary rock in a
such as passive continental margin (Gross and Mcleod, 1980).

Although the resources of Neoproterozoic BIFs are even much less than those of Archean and Paleoproterozoic, they are widely distributed worldwide, such as Rapitan BIF in Canada (Halverson et al., 2011), Wadi Karim and Um Anab BIF in Egypt (Basta et al., 2011), Sawawin BIF in Saudi Arabia (Stern et al., 2013), Jacadigo in Brazil (Freitas et al., 2011), Holowilena and Oraparinna in South Australia (Cox et al., 2016), the Kingston Peak Formation in California (Lechte et al., 2018) and Wadi Hamama in the Arabian Nubian Shield (El-Rahman et al., 2020). They were also discovered in the Precambrian massifs in Phanerozoic orogenic belts of South China, such as Sanjiang in Guangxi Province (Yan et al., 2010), Shilu in Hainan Province (Xu et al., 2014), Xinyu in Jiangxi Province (Li et al., 2014; Shen et al., 2018; Zhu et al., 2019), the Shalong in the Central Tianshan (Lei et al., 2016, 2018) and Dahongliutan BIF in the Western Kunlun orogenic belt (Hu et al., 2017, 2020). Several

im
at the
asement
articul
ightl
ing

2

These samples are dominated by magnetite an
mesoband (mm- to cm-scale) and microban
magnetite, quartz, rare hematite, siderite,
minerals, such as chlorite (Fig. 3g) and se
the bedding.

The shallow gray tuffs under th
Nevertheless, the sub-euhedral or
mm, can be seen under magnif
sample was collected from
(

The blackish green b
The minerals in the
oxide can be ob
geochemical an

4 Analyti

**4.1 **

**4.2 **
Seve
location. Wh
fused glass beads
Survey), following the
uncertainties are between 1 and
Fe_2O_3, with the procedures described
supplementary Table 2.

Trace elements were determined using a Perkin-Elmer Sci N DI
ratory of Ore Deposit Geochemistry, Institute of Geochemis (C
lytical accuracy better than 5%. Samples were d d with 1m
TEE-lined stainless steel bombs at 190 2h (Qi et al., 2000). The
tter than 1% with co s > 200 ppm, and 1-3% when less
pplementary Table 2.
ass Isoprobe M ICP-MS at Tianjin
Institut hina Geological Su
similar to t Measured $^{87}Sr/^{86}Sr$ an
for mass-fraction .1194 and $^{146}Nd/^{144}Nd = 0$.
values for the NBS dard $^{87}Sr/^{86}Sr$ = 0.71025 and
$^{143}Nd/^{144}Nd$ = 0.512115. All tial $^{143}Nd/^{144}Nd$ values of the BIF a
depositional age (737 Ma) for th iijanshan BIF.

Iron isotope ratios were m MC-ICP-MS at Beijing Createch Tes
Ltd. The results of Fe iso he ten thousandth deviation of t
the standard sample is

of
were
ated in
s can be
erally have
MSWD=5.8).
onstruct a good
Discordia with an intercepted age of 736.2±3.8 Ma (N=21, Fig. 4). Excluded
the significant discordant analyses, the left fifteen analyses of well concordance be $^{206}Pb/^{238}U$ age
and $^{207}Pb/^{235}U$ age, yield a mean $^{206}Pb/^{238}U$ age of 737.0±4.0 Ma (N=15, MSW
interpreted as the deposition time of the Baijianshan BIF.

5.2 Whole rock Geochemistry
5.2.1 Geochemistry of the basalts
Three basalt samples (2702H1, 270H2 and 2702H3) have low S
The incompatible elements for the rock type classification are u
Nb/Y ratios (1.05-1.09) define their alkaline signature and in t
into the alkaline basalt field (Figure not shown). With respe
ranging from 186 ppm to 195 ppm and show variable LR
(Fig. 5a) (La$_N$/Yb$_N$ = 9.8-11.0). In line with their low
ppm), the basalts are evolved magma. However, the
features of the OIB-like basalts with insignificant N

5.2.2 Geochemistry of the BIF
As shown in supplementary Table 2, the s
Fe$_2$O$_3^T$ concentrations vary between 13.1
between 26.81% and 55.06% (42.02%
3.66% on average), TiO$_2$, MnO, P$_2$O$_5$
incompatible elements (supplement

Their REE abundances vary fr
Shale (PAAS; McLennan, 198
the La$_N$/Yb$_N$ of 0.23-0.69 (Fi
of Ce/Ce* ~ 1 and Pr/Pr*
0.96-1.14; Y/Ho ratios

5.2.3 Sr-Nd isotop
Sr-Nd concen
supplementary
($^{87}Sr/^{86}Sr$)$_i$

6.9.
Str
fro
(

5.2.4 Fe isotope com
The Fe isotope compositions of the Baijianshan B
The six samples yield $^{56}Fe_{IRMM-014}$ values of 1.24- $^{57}Fe_{IRMM-014}$ values of 1.78
Their enrichment in heavy Fe isotopes shares the signatures of the Neoproterozoic BIFs (Halverson et
al., 2011; Yan et al., 2011; Shen et al., 2018).

6 Discussions

6.1 Iron sources for the Baijianshan BIFs
Field and microscopic observations revealed that the Neoproterozoic Baijianshan BIF has not

experienced significant metamorphism (Fig. 3b, c and d), indicating the original geochemical characteristics were well retained and can be used to decipher the iron sources and the oceanic environments when it precipitated.

The Baijianshan BIF shows a modern seawater REE signature with significant LREE depletion relative to the HREE ($La_N/Yb_N = 0.41$) (Fig. 5b, Zhang and Nozaki, 1996; Alibo and Nozaki, 1999). A range of factors can affect the primary REY composition in terms of BIF depositional processes, including post-depositional metamorphism and/or syn-deposition clastic contamination (Alexander et al., 2008; Hu et al., 2020). Previous studies demonstrated that diagenetic and metamorphic events (such as weathering and/or fluid-rock interactions) have negligible effects on the REY of the chemical sediments (Bolhar et al., 2004). However, Rb is a relatively mobile element compared to highly immobile elements such as Th. In Fig. 6a, the well positive correlation between Rb and Th demonstrates insignificant mobility of the LILEs (Large Ion Lithophile Elements) and the absence of significant diagenetic or metamorphic alteration effects, this conclusion is also consistent with thin section observations (Fig. 3c, d, g, h). With respect to the syn-depositional processes, the contents of Al_2O_3 and TiO_2 are consistently low with averages of 3.66% and 0.41%. In addition, despite the positive correlations between Al_2O_3 and TiO_2 (r = 0.93), K_2O (r = 0.79), Rb (r = 0.78), V (r = 0.45), Sc REE (r = 0.62) (Fig. 6b-i) signify the incorporation of terrigenous contribution in the deposition processes, most correlation coefficients are much lower than those BIFs sourced from recycled crust (Basta et al., 2011; Cox et al., 2013; Hu et al., 2017, 2020). Besides, the Baijianshan BIF shares similar REE patterns with those BIFs from North China Craton but contains slightly higher contents of Al_2O_3 and TiO_2 (Li et al., 2014). Taken together, we suggest a little incorporation of terrigenous component in the Baijianshan BIF.

Positive Eu anomalies are generally interpreted as the precipitation of high-temperature hydrothermal fluids (Danielson et al., 1992; Bau and Dulski, 1999) while low-temperature hydrothermal fluids usually display weak or no Eu anomalies (Michard et al., 1993; Li et al., 2014). Most samples from the Baijianshan BIF show negligible Eu anomalies (Eu/Eu* = 0.96~1.14, averaging 1.07), which are indicative of low-temperature hydrothermal solutions (Danielson et al., 1992). The (t) value can be used as a tracer to distinguish different sources and crustal contamination. As shown in Fig. 7, the Baijianshan BIF has slightly average (t) value (average of 0.37), much lower than those of Baijianshan basalt, indicating that the deposition of the Baijianshan BIF was controlled by a hydrothermal flux with mantle- (Jacobsen and Pimentel-Klose, 1988). However, the slightly negative correlation between Ma) and Al_2O_3 contents (Fig. 8a) argues for the low proportion of detrital components inputting.

The Y/Ho ratios of BIFs can provide constraints of the material source and precipitation environment of BIFs (Hu et al., 2017). Modern seawaters have a Y/Ho ratio of 44-74 (Bau and Dulski, 1996). The terrestrial material has a Y/Ho ratio of ~26, any little terrestrial contamination could quickly descend seawater-like superchondretic Y/Ho ratios (>44) (Bolhar et al., 2004). The hydrothermal fluids have almost chondritic Y/Ho ratios (26-28, Douville et al., 1999; Bau and Dulski, 1999). The Baijianshan BIF has a range of Y/Ho ratios between 23 and 32, similar to the chondritic values (26-28, Bau and Dulski, 1999), possibly due to the mixture of high and/or low-T hydrothermal fluids (Hu et al., 2020). Y/Ho ratios of the Baijianshan BIF samples might inherit from the low-T hydrothermal fluids, but the influences of terrestrial materials can not be completely excluded. Compared with the BIFs in North China Craton, the Baijianshan BIF displays relatively low positive Eu anomalies, low Y/Ho ratios as well as a slighly depleted Li et al., 2014; Wang et al., 2016), illustrating the input of low-temperature hydrothermal fluids during the deposition of the Baijianshan BIF.

$Ce/Ce^*{}_{PAAS}$ values with variable Al_2O_3 contents of the Baijianshan BIF indicate that terrigenous detrital materials played little role in the geochemical budget of Ce. In oxidized seawater, Ce(Ⅲ) transforms into Ce(Ⅳ), and then Ce(Ⅳ) is likely to be hydrolyzed and precipitated with Fe-Mn oxyhydroxides, organics and clay which lead to a significant negative Ce anomaly of seawater (Byrne and Sholkovitz, 1996). As shown in the Ce/Ce^* vs. Pr/Pr^* diagram (Fig. 10), all the Baijianshan BIF samples display no Ce anomalies, similar with most Neoproterozoic BIFs, unambiguously arguing for anoxic environment in the ancient ocean. Although the atmospheric and oceanic oxygen levels during the Neoproterozoic are still under debate, numerous studies revealed that Neoproterozoic oceans underwent a stepwise and protracted oxidation. Anoxic ferruginous deep seawater was a typical feature of the late Neoproterozoic, as inferred from geochemical proxies such as iron geochemistry (e.g., Canfield et al., 2008; Sperling et al., 2015), redox-sensitive elements (e.g., Schröder and Grotzinger, 2007; Rajabi et al., 2015), and framboidal pyrite (e.g., Rajabi et al., 2015). Stern et al. (2013) suggested that this scenario might be attributed to the seawater surfaces being covered by ice sheets, blocking the oxygen from atmosphere dissolving into the widespread anoxic ferruginous ocean. Despite no tillite was identified at the Baijianshan BIF, the coeval tillite sequences were documented in the Quruqtagh area (i.e., ca.740 Ma Beiyixi tillite) of NE Tarim (Xu et al., 2009), which argued for the possibility of ice sheets in the Cryogenian Baijianshan ocean.

In a Fe^{2+}-rich marine settings, both abiotic and biotic action were demonstrated as oxidation pathways for the precipitation of iron oxyhydroxides ($Fe(OH)_3$) from dissolved Fe^{2+} (Konhauser et al., 2011). As an element of variable valency, the fractionation of Fe isotope is affected by the oxidation-reduction condition (Bullen et al., 2001; Zhu et al., 2002; Balci et al., 2006). Experimental studies demonstrated that oxidation of Fe^{2+} to Fe^{3+} in solution causes considerable Fe isotope fraction, generating an enrichment of heavy Fe isotopes in Fe^{3+} (Bullen et al., 2001; Johnson et al., 2002; Balci et al., 2006; Hou et al., 2014). On the other hand, the fractionation caused by pyrite with light-Fe isotopes is considered to play a leading role in the enrichment of heavy Fe isotopes in the residual system relative to the original state (Rouxel et al., 2016), since the pyrite is easier to precipitation from plume. Nevertheless, there is no sulfide observed in the Baijianshan BIF, thus the potential influences of sulfides on the enrichment of heavy Fe isotopes can be excluded. Under oxidized environment, the enrichment of heavy Fe isotopes is shown in oxide or hydroxide of iron trivalent ($Fe^{3+}{}_{ppt}$) and light Fe isotope is displayed in Ferrous solution ($Fe^{2+}{}_{aq}$) (Johnson et al., 2002). The magnitude of Fe isotope fractionation is controlled by the degree of precipitation from Fe^{2+} to Fe^{3+}, which is related to the degree of ocean oxidation (Yan et al, 2010). The Fe in the seawater can be completely precipitated and no fractionation of the Fe isotope occurs when the seawater is completely oxidized, thus the Fe isotope values in iron oxide precipitates (Fe^{3+}) can represent the Fe isotope information of seawater. However, when the seawater is partially oxidized, the Fe in the seawater is partially precipitated and the Fe isotope fractionation will occur in iron oxide precipitates (Fe^{3+}). Therefore, the Fe isotope value can be used as a proxy to decipher the redox state of seawater (Yan et al., 2010). Compared with some BIFs deposited during the Archean-Paleoproterozoic (Dauphas et al., 2004; Rouxel et al., 2005; Li et al., 2012; Johnson et al., 2003; Hou et al., 2014; Li et al., 2014), the Neoproterozoic Baijianshan Sanjiang (Yan et al., 2010) and Xinyu BIFs (Shen et al., 2008) have higher values ^{57}Fe (Fig. 11). Several studies demonstrated that the low ^{57}Fe values of BIFs could be due to the contributions from a continental component and the continental Fe source is best explained by Fe mobilization on the continental margin by microbial dissimilatiry iron reduction (DIR) (Johnson et al., 2008; Li et al., 2015). As for the Fe isotope values of Archean-Paleoproterozoic BIFs we cited, the Fe source of SW Greenland BIF, Anshan-Benxi BIFs, Gongchangling BIFs and Yuanjiacun BIFs are unambiguously demonstrated to be hydrothermal type similar to the scenario of the Baijianshan BIF (Dauphas et al., 2004; Li et al., 2012; Li et al., 2014; Hou et al., 2014), while the Fe of Transvaal, Manjeri, Belingwe Belt and Zimbabwe BIFs are probably from multiple sources (abiologic and biologic processes) (Johnson et al., 2008; Grassineau et al., 2011). The comparison reveals that the environment in which they precipitated was more reduced. Both the iron isotope and elemental geochemistry thus demonstrate that the Neoproterozoic Baijianshan ocean might have the same reduced environment as Archean or Paleoproterozoic, or even more reduced.

6.3 A model of the Baijianshan BIF

During the late Neoproterozoic period (i.e., 750-550 Ma), the Earth experienced long-lived global glaciations, known as the Snowball Earth events (Hoffman et al., 1998). In view of the Neoproterozoic oxygenation event (NOE) at that time, the content of oxygen in atmosphere was much higher than before (Och et al., 2012). Recently, EI-Rahman et al. (2020) argued that some Neoproterozoic BIFs are not glaciogenic due to their significant depleted Nd isotope compositions. Under this scenario, the iron was most likely deriving from hydrothermal alteration of juvenile oceanic crust. The Chondritic-like Nd isotope compositions of the Baijianshan BIF (do not favor this model. Furthermore, the close temporally-spatially related tillite sequences in the Quruqtagh of NE Tarim (Xu et al., 2009), 765 Ma-735 Ma tillites in Namibia, suggested a local glaciation termed as Kaigas

glaciation (Kay et al., 2001; Cailteux et al., 2005; Hoffmann et al., 2006). Considering the high latitude position of the Tarim in the Rodinia configuration (Li et al., 2008), the Kaigas glaciation (corresponding to the Beiyixi tillite in Tarim) most possibly occurred in Tarim. In combination with previous studies on other BIFs with the data presented in this study, we construct a cartoon model showing the formation mechanism of the Baijianshan BIF (Fig. 12).

Stage 1, the seawater was covered by ice sheet which led to the insulation between atmosphere and oceans with the in   And then it induced the emergence of a reductive ocean. The iron supplied by low-temperature hydrothermal fluids could exist as the ferrous form, forming a relatively stable anoxic ferruginous reservoir in the ocean.

Stage 2, at interglacial period, the partial melting of the ice sheet caused some oxygen from the atmosphere into the ocean, which emerged a stratified seawater. There were mainly anoxic and Fe^{2+}-rich deeper seawater, whereas the Fe^{2+} was gradually oxidized into Fe^{3+} and precipitated into iron oxide in near-shore oxic shallow seawaters. The low-temperature hydrothermal was the dominant source during the precipitation process to interpret the slight positive Eu anomalies and positive values   . Under the effect of the melting ice-sheet, the increasing weathering then contributed to a small amount of terrestrial materials into the shallow seawater, resulting the precipitation of the Baijianshan BIF.

7 Conclusions

The Baijianshan BIF precipitated in glacially-influenced settings during the Neoproterozoic (737 Ma). Low-T hydrothermal fluids, accompanied with limited detritus input, were the dominated iron sources for the formation of Baijianshan BIF.

The Baijianshan ocean was initially covered by ice sheets, giving rise to the extremely reduced environment favored by Fe^{2+}. Then it was oxidized into Fe^{3+} and precipitated as magnetite due to the thawing of ice sheets. At the early stage, local reduced ocean enhanced Fe fluxes genetically related to the intensive marine magmatism and hydrothermal activities due to the existence of ice sheets. Thawing of ice sheets induced oxidized oceanic layer, favoring the formation of the Neoproterozoic BIF at the later stage.

Acknowledgements

References
Alexander, B.W., Bau, M., Andersson, P., Dulski, P., 2008. Continentally-derived solutes in shallow Archean seawater: rare earth element and Nd isotope evidence in iron formation from the 2.9 Ga Pongola Supergroup, South Africa. Geochim. Cosmochim. Acta 72, 378-394.
Alibo, D.S., Nozaki, Y., 1999. Rare earth elements in seawater: particle association, shale normalization and Ce oxidation. Geochim. Cosmochim. Acta 63(3-4), 363-372.
Andrade, S., Hypolito, R., Ulbrich, H.H.G.J., Silva, M.L., 2002. Iron(Ⅱ) oxide determination in rocks and minerals. Chem. Geol. 182, 85-89.
Balci, N., Bullen, T.D., Witte-Lien, K, Shanks, W.C., Motelica, M., Mandernack, K.W., 2006. Iron isotope fractionation during microbially stimulated Fe(Ⅱ) oxidation and Fe(Ⅲ) precipitation. Geochim Cosmochim Acta 70, 622-639.
Basta, F.F., Maurice, A.E., Fontboté, L., Favarger, P.Y., 2011. Petrology and geochemistry of the banded iron formation (BIF) of Wadi Karim and UmAnab, Eastern Desert, Egypt: implications for the origin of Neoproterozoic BIF. Precambrian Res. 187, 277-292.
Bau, M., Dulski, P., 1996. Distribution of yttrium and rare-earth elements in the Penge and Kuruman iron-formations, Transvaal Super group, South Africa. Precambrian Res. 79, 37-55.
Bau, M., Dulski, P., 1999. Comparing yttrium and rare earths in hydrothermal fluids from the Mid-Atlantic Ridge: implications for Y and REE behaviour during nearvent mixing and for the Y/Ho ratio of Proterozoic seawater. Chem. Geol. 155, 77-90.
Bolhar, R., Kamber, BS., Moorbath, S., Fedo, C.M., Whitehouse, M.J., 2004. Characterisation of early Archaean chemical sediments by trace element signatures. Earth Planet. Sci. Lett. 222, 43-60.
Bullen, T.D., White, A.F., Childs, C.W., Vivit, D.V., Schulz, M.S., 2001. Demonstration of significant abiotic iron isotope fractionation. Geology 29, 699-702.
Byrne, R., Sholkovitz., 1996. Marine chemistry and geochemistry of the lanthanides. In: Gschneider Jr.K.A., Eyring, L. (Eds.), Handbook on the Physics and Chemistry of the Rare Earths. Elsevier, Amsterdam.
Cailteux, J.L.H., Kampunzu, A.B.H., Batumike, M.J., 2005. Lithostratigraphic position and petrographic - Journal of African Earth Sciences 42, 82-94.
Canfield, D.E., Poulton, S.W., Knoll, A.H., Narbonne, G.M., Ross, G., Goldberg, T., Strauss, H., 2008. Ferruginous Conditions Dominated Later Neoproterozoic Deep-Water Chemistry. Science 321(5891), 949-952.
Chen, D.Z., Wang, J.G., Qing, H.R., Yan, D.T., Li, R.W., 2009. Hydrothermal venting activities in the Early

Cambrian, South China: Petrological, geochronological and stable isotopic constraints. Chemical Geology 258, 168-181.

Cox, G.M., Halverson, G.P., Minarik, W.G., Heron, D.P.L., Macdonald, F.A., Bellefroid, E.J., Strauss, J.V., 2013. Neoproterozoic iron formation: an evaluation of its temporal, environment al and tectonic significance. Chem. Geol. 362, 232-249.

Cox, G.M., Halverson, G.P., Poirier, A., Le Heron, D., Strauss, J.V., Stevenson, R., 2016. A model for Cryogenian iron formation. Earth Planet. Sci. Lett. 433, 280-292.

Danielson, A., Moller, P., Dulski, P., 1992. The europium anomalies in banded iron formations and the thermal history of the oceanic crust. Chem. Geol. 97, 89-100.

Dauphas, N., van Zuilen, M., Wadhwa, M., Davis, A.M., Marty, B., Janney, P.E., 2004. Clues from Fe isotope variations on the origin of early Archean BIFs from Greenland. Science 306, 2077-2080.

EI-Rahman, Y.A., Gutzmer, J., Li, X.H., Seifert, T., Li, C.F., Ling, X.X., Li, J., 2020. Not all Neoproterozoic iron formations are glaciogenic: Sturtian-aged non-Rapitan exhalative iron formations from the Arabian-Nubian Shield. Mineralium Deposita 55, 577-596.

Feng, L.J., Huang, J., Lu, D.B., Zhang, Q.R., 2016. Major and trace element geochemistry of the Neoproterozoic syn-glacial Fulu iron formation, South China. Geological Magazine 154, 1-10.

Freitas, B.T., Warren, L.V., Boggiani, P.C., Almeida, R.P.D., Piacentini, T., 2011. Tectono-sedimentary evolution of the Neoproterozoic BIF-bearing Jacadigo Group, SW-Brazil. Sedimentary Geology 238, 48-70.

Grassineau, N.V., Nisbet, E.G., Bickle, M.J., Fowler, C.M.R., Lowry, D., Mattey, D.P., Abell, P., Martin, A., 2000. Antiquity of the biological sulphur cycle: evidence from sulphur and carbon isotopes in 2700 million-year-old rocks of the Belingwe Belt, Zimbabwe. Proc. R. Soc. Lond. B 268, 113-119.

Gross, G.A., 1980. A classification of iron-formation based on depositional environments. Canadian Mineralogist 18, 215-222.

Gross, G.A., Mcleod, C.R., 1980. A preliminary assessment of the chemical composition of iron formation in Canada. Canadian Mineralogist 18, 223-229.

Halverson, G.P., Poitrasson, F., Hoffman, P.F., Nédélec, A., Montel, J.M., Kirby, J., 2011. Fe isotope and trace element geochemistry of the Neoproterozoic syn-glacial Rapitan iron formation. Earth Planet. Sci. Lett. 309(1), 100-112.

Hoffman, P.F., Kaufman, A.J., Halverson, G.P., Schrag, D.P., 1998. A Neoproterozoic snowball Earth. Science 281, 1342-1346.

Hoffman, P.F., Schrag, D.P., 2002. The snowball earth hypothesis: testing the limits of global change. Terra Nova 14(3), 129-155.

Hoffmann, K.H., Condon, D.J., Bowring, S.A., Prave, A.R., Fallick, A., 2006. Lithostratigraphic, carbon (^{13}C) isotope and U-Pb zircon age constraints on early Neoproterozoic (ca. 755 Ma) glaciation in the Gariep Belt, southern Namibia. Snowball Earth Conference, July 16-21, 2006, Montle Namibia, Ticino, Switzerland, 51.

Holland, H.D., 2002. Volcanic gases, black smokers, and the great oxidation event. Geochimica et Cosmochimica Acta 66(21), 3811-3826.

Hou, K.J., Li, Y.H., Gao, J.F., Liu, F., Qin, Y., 2014. Geochemistry and Si-O-Fe isotope constraint on the origin of banded iron formations of the Yuanjiacun Formation, Lvliang Group, Shanxi, China. Ore Geology Reviews 57, 288-298.

Hu, J., Wang, H., Wang, M., 2017. Geochemistry and origin of the Neoproterozoic Dahongliutan banded iron formation (BIF) in the Western Kunlun orogenic belt, Xinjiang (NW China). Ore Geology Reviews 89, 836-857.

Hu, J., Wang, H., Zhang, L.G., 2020. A rare earth element and Nd isotopic investigation into the provenance and deposition of the Dahongliutan banded iron formation and associated carbonates, NW China: Implications on Neoproterozoic seawater compositions. Precambrian Research 342, 1-29.

Jackson, S.E., Pearson, N.J., Griffin, W.L., Belousova, E.A., 2004. The application of laser ablation-inductively coupled plasma-mass spectrometry to in situ U Pb zircon geochronology. Chemical Geology 211(1-2), 47-69.

Jacobsen, S.B., Pimentel-Klose, M.R., 1988. Nd isotopic variations in Precambrian banded iron formations. Geophys Res Lett 15, 393-396.

James, H.L., 1954. Sedimentary facies of iron-formation. Economic Geology 49(3), 235-293.

James, H.L., 1966. Chemistry of the iron-rich sedimentary rocks. U.S. Geol. Survey Prof, 440-461.

James, H.L., 1983. Distribution of banded iron-formation in space and time. Developments in Precambrian Geology 6, 471-490.

Johnson, C.M., Beard, B.L., Beukes, N.J.,
Earth as inferred from Fe isotope studies of banded iron formations from the Transvaal Craton. Contributions to Mineralogy and Petrology 144(5), 523-547.

Johnson, C.M., Beard, B.L., Klein, C., Beukes, N.J., Roden, E.E., 2008. Iron isotopes constrain biologic and abiologic processes in banded iron formation genesis. Geochimica Et Cosmochimica Acta 72(1), 151-169.

Johnson, C.M., Skulan, J.L., Beard, B.L., Sun, H., Nealson, K.H., Braterman, P.S., 2002. Isotopic fractionation between Fe(Ⅲ) and Fe(Ⅱ) in aqueous solution. Earth Planet Sci Lett 195, 141-153.

Johnston, D.T., Poulton, S.W., Dehler, C., Porter, S., Husson, J., Canfield, D.E., Knoll, A.H., 2010. An emerging picture of Neoproterozoic ocean chemistry: insights from the Chuar Group, Grand Canyon, USA. Earth Planet. Sci. Lett. 290, 64-73.

Kay, R.M., Liyungu, A.K., Njamu, F.M., Somwe, V., Banda, J., Mosley, P.N., Armstrong, R.A., 2001. The western arm of the Lufilian Arc in NW Zambia and its potential for copper mineralization. Journal of African Earth Sciences 33, 503-528.

Klein, C., 2005. Some Precambrian banded iron-formations (BIFs) from around the world: Their age, geologic setting, mineralogy, metamorphism, geochemistry, and origins. American Mineralogist 90(10), 1473-1499.

Klein, C., Beukes, N.J., 1992. Time distribution, stratigraphy, sedimentologic setting, and geochemistry of Precambrian iron-formations. In: Schopf, J.W., Klein, C. (Eds.), The Proterozoic Biosphere. Cambridge University Press, Cambridge, 139-146.

Klein, C., Ladeira, E.A., 2004. Geochemistry and mineralogy of Neoproterozoic banded iron-formations and some selected, siliceous manganese formations from the Urucum district, Mato Grosso do Sul, Brazil. Econ. Geol. 99, 1233-1244.

Konhauser, K.O., Kappler, A.K., Roden, E.E., 2011. The microbial role in iron redox and biomineralization reactions. Elements 7, 89-93.

8

change. Precambr. Res. 239, 79-94.

Sun, S.S., McDonough, W.F., 1989. Chemical and isotopic systematics of oceanic basalts: Implications for mantle composition and processes. Geological Society London Special Publications 42(1), 313-345.

Tang, S.H., Zhu, X.K., Li, J., Yan, B., Li, S.Z., Li, Z.H., Wang, Y., Sun, J., 2016. New Standard Solutions for Measurement of Iron, Copper and Zine Isotope Compositions by Multi-collector Inductively Coupled Plasma-Mass Spectrometry. ROCK AND MINERAL ANALYSIS 35(2), 127-133 (in Chinese with English abstract).

Wu, Y.B., Zheng, Y.F., 2004. A study on the genetic mineralogy of zircon and its restriction on the interpretation of U-Pb age. CHINESE SCIENCE BULLETIN 49(16), 1589 (in Chinese).

Xinjiang Bureau of Geology and Mineral Resources (BGMR), 1993. Regional Geology of Xinjiang Uygur Autonomous Region. Geological Publishing House, Beijing, 8-33 (in Chinese).

Xu, B., Xiao, S.H., Zou, H.B., Chen, Y., Li, Z.X., Song, B., Liu, D.Y., Zhou, C.M., Yuan, X.L., 2009. SHRIMP zircon U-Pb age constraints on Neoproterozoic Quruqtagh diamictites in NW China. Precambrian Research 168, 247-258.

Xu, B., Zou, H.B., Chen, Y., He, J.Y., Wang, Y., 2013. The Sugetbrak basalts from northwestern Tarim Block of northwest China: Geochronology, geochemistry and implications for Rodinia breakup and ice age in the Late Neoproterozoic. Precambrian Research 236, 214-226.

Xu, D.R., Wang, Z.L., Chen, H.Y., Hollings, Pete, Jansen, Nicholas, H., Zhang, Z.C., Wu, C.J., 2014. Petrography and geochemistry of the Shilu Fe Co Cu ore district, South China: Implications for the origin of a Neoproterozoic BIF system. Ore Geology Reviews 57, 322-350.

Xu, Z.Q., He, B.Z., Zhang, C.L., Zhang, J.X., 2013. Tectonic framework and crustal evolution of the Precambrian basement of the Tarim Block in NW China: New geochronological evidence from deep drilling samples. Precambrian Research 235, 150-162.

Yan, B., Zhu, X.K., Tang, S.H., Zhu, M.Y., 2010. Fe isotopic characteristics of the Neoproterozoic BIF in Guangxi Province and its Implications
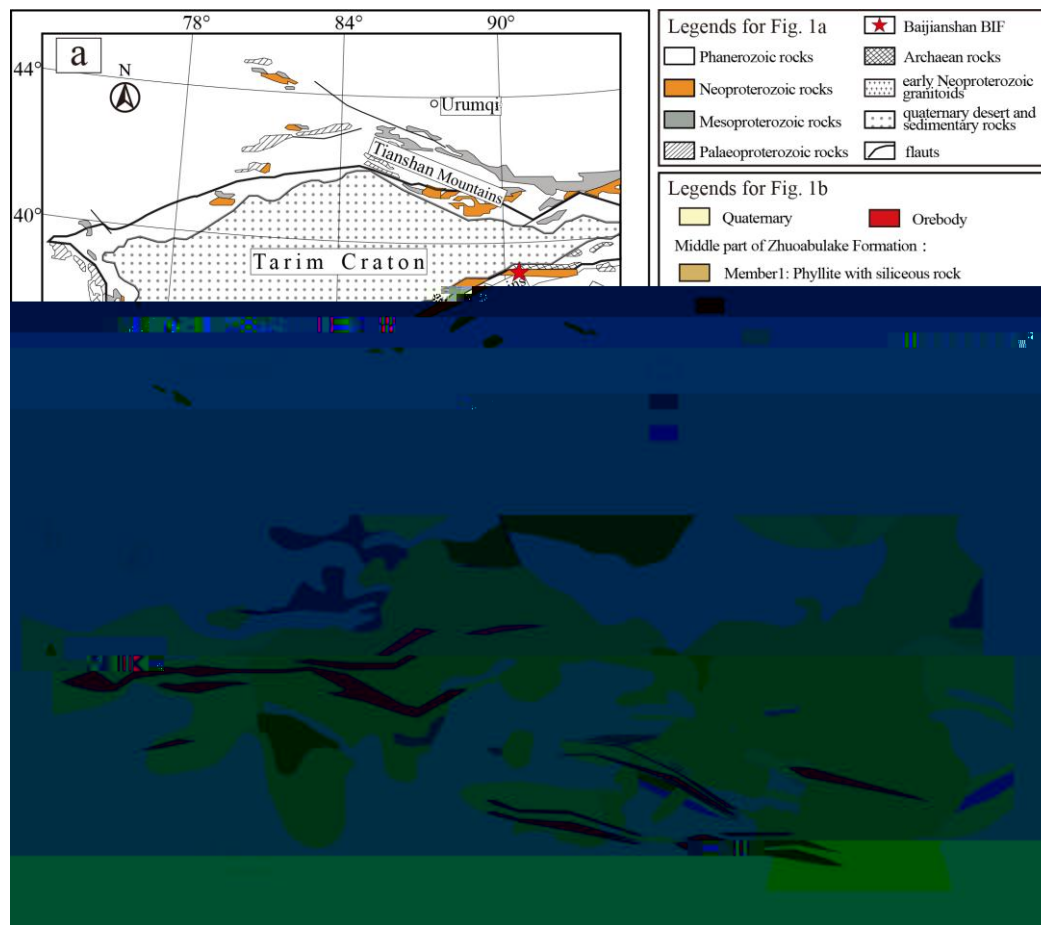
Figure captions

Fig. 1 (a) Sketch Precambrian geological map of Tarim Craton, showing the location of the Baijianshan BIF (modified after Lu et al., 2008). (b) Geological map of the Baijianshan Banded Iron Formation (Baijianshan BIF).
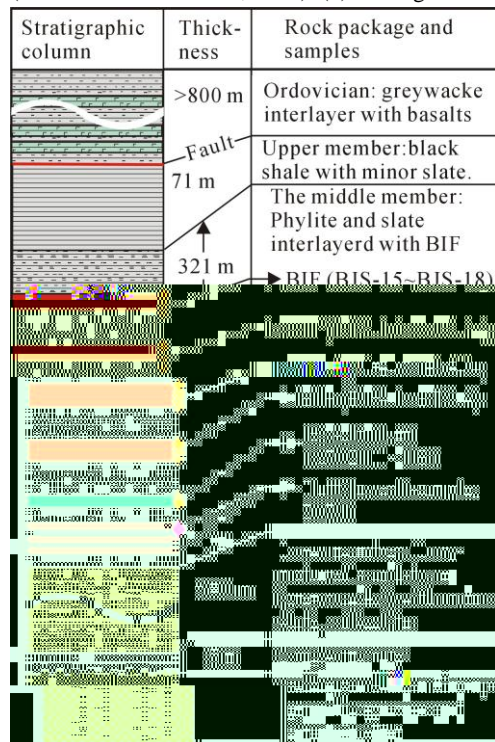
Fig. 2 Stratigraphical column of the Baijianshan BIF.
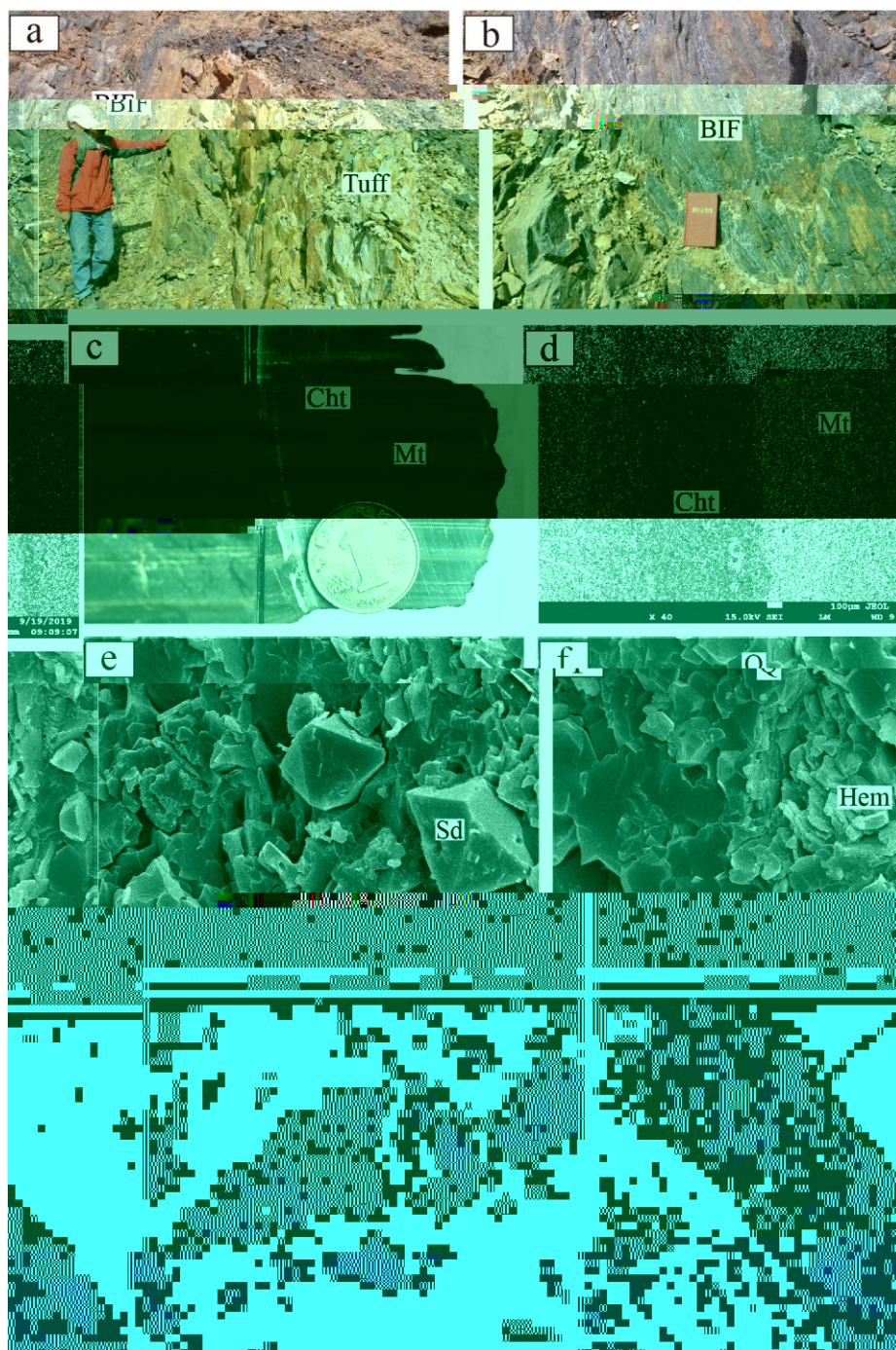
Fig. 3 Field photographs, hand specimen and mineral features of the Baijianshan BIF. (a) The tuff layers in the Baijianshan BIF. (b) Laminated Fe orebodies with local bend. (c) hand specimen. (d) Scanning electron microscopy (SEM) images. Detailed petrographic examination by SEM and transmitted light showing mineral assemblage: (e) Siderite. (f) Hematite. (g) Chlorite. (h) Sericite. Cht = Chert, Mt = Magnetite, Sd = Siderite, Q = Quartz, Hem = Hematite, Chl = Chlorite, Ser = Sericite.

12
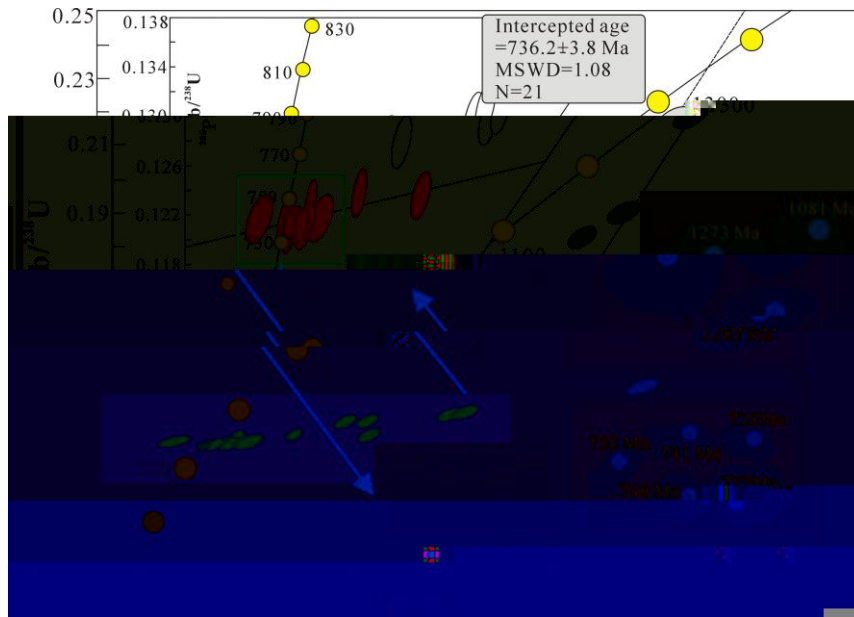
Fig. 4 Concordia diagram of the zircon U-Pb ages of the tuff at the Baijianshan BIF.
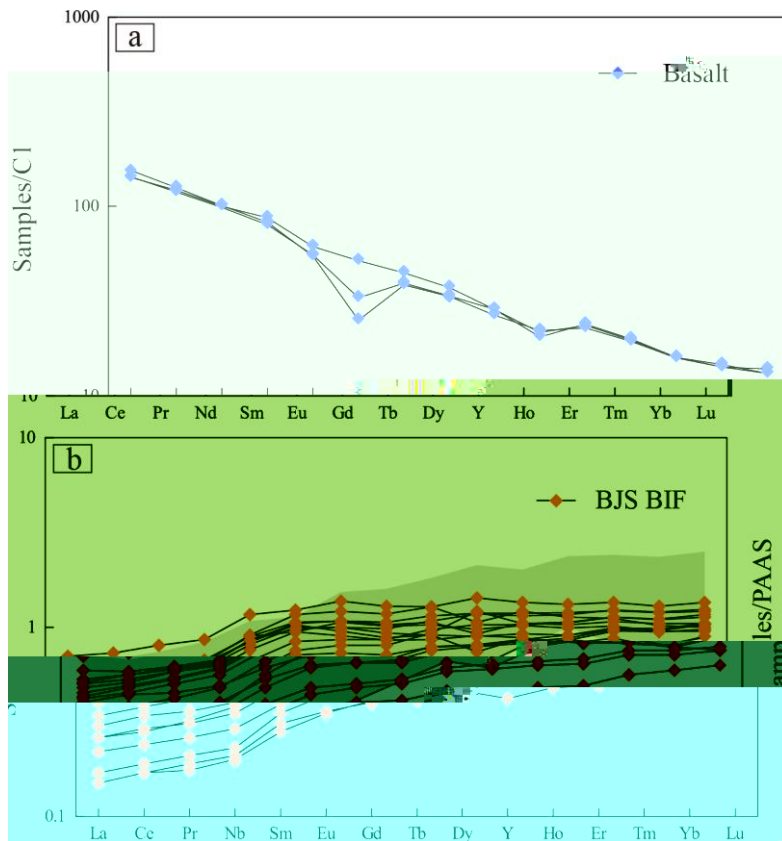
Fig. 5 (a) Chondrite-normalized REE parttern of the basalts. Chondrite-normalized values after Sun and McDonough (1989). (b) PAAS-normalized REE+Y diagrams of BIFs from the Baijianshan BIF. The grayish zone represents the REY data from the Xinyu BIF (Li et al., 2014). PAAS-normalized values after McLennan (1989).

13
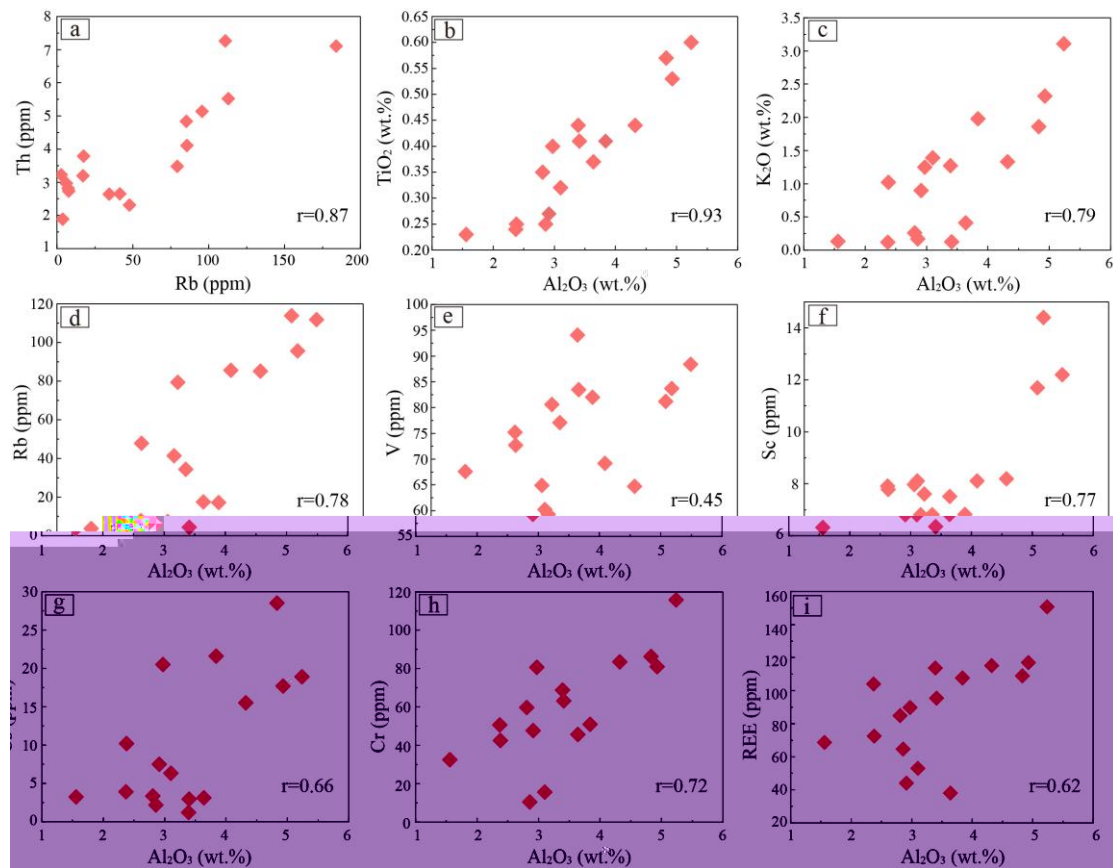
Fig. 6 (a) Bi-variation n between Rb and Th of Baijianshan BIF samples; (b-i) Bi-variation between Al_2O_3 and TiO_2 (b), K_2O (c), Rb (d), V (e), Sc (f), Cs (g), Cr (h) and REE (i) of the Baijianshan BIF. Data for bulk-rock BIF samples are listed in supplementary Table 2.
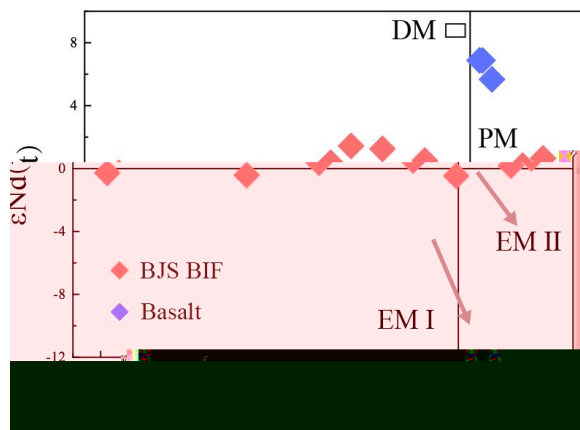
Fig. 7 $^{87}Sr/^{86}Sr)_i$ diagram of BIF and basalt samples in Baijianshan.
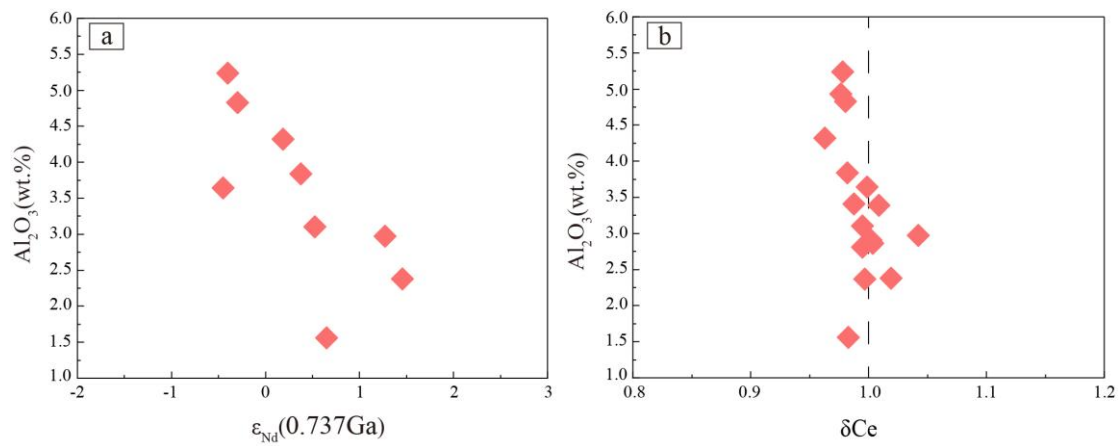
Fig. 8　　　　　(t = 0.737Ga) vs. Al$_2$O$_3$ diagram of the Baijianshan BIF; (b) Ce/Ce$^*_{PAAS}$ vs. Al$_2$O$_3$ diagram of the Baijianshan BIF.
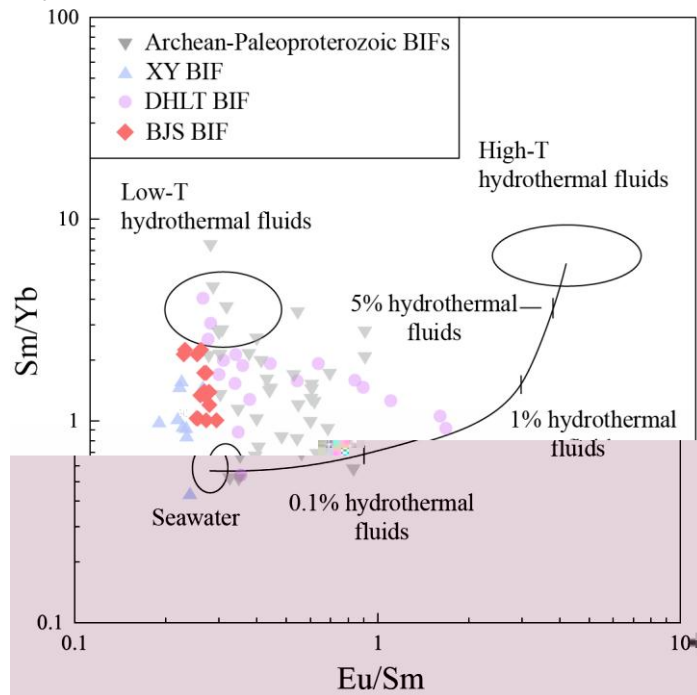
Fig. 9 Sm/Yb vs. Eu/Sm ratios illustrating two component mixing model of the hydrothermal fluid of the Baijianshan BIF (after Alexander et al., 2008). BJS-Baijianshan BIF; XY-Xinyu BIF (Li et al., 2014); DHLT-Dahongliutan BIF (Hu et al., 2017). Data sets of Archean-Paleoproterozoic BIFs are from Planavsky et al. (2010). Average compositions of high-T (> 300 °C) hydrothermal fluids, low-T (< 200 °C) hydrothermal solutions and Pacific seawaters were after Bau and Dulski (1999), Michard et al. (1983) and Alibo and Nozaki (1999), respectively.
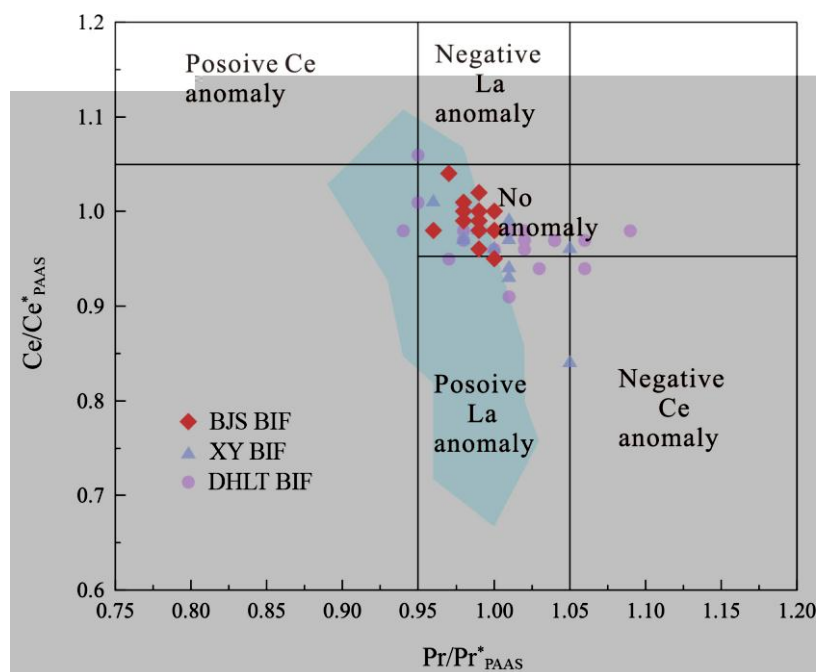
Fig. 10 Pr/Pr*$_{PAAS}$ vs. Ce/Ce*$_{PAAS}$ diagram for the BIF at Baijianshan (after Bau and Dulski, 1996). The light blue area represents the data of Archean-Paleoproterozoic BIFs. Data sets of other BIFs are same as those of Fig. 9.
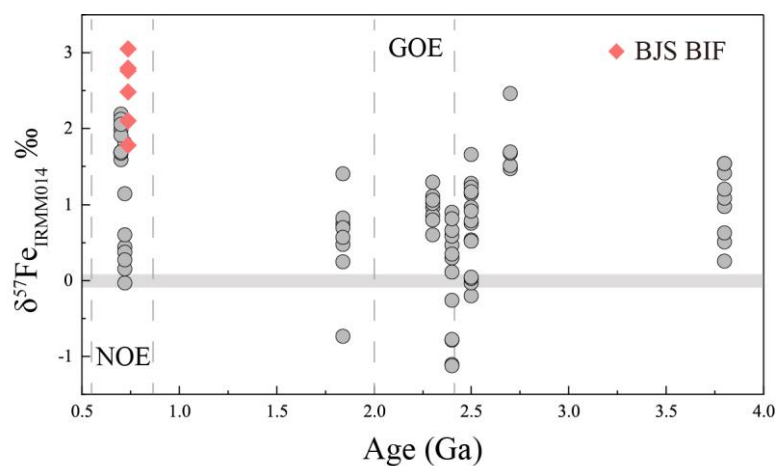
Fig. 11 ^{57}Fe$_{IRMM-014}$ of various ages BIFs in the world (Data of SW Greenland BIFs are from Dauphas et al.(2004); Manjeri Formation, Belingwe Belt, Zimbabwe BIFs are from Rouxel et al. (2005); Anshan-Benxi BIFs are from Li et al. (2012); Transvaal BIFs are from Johnson et al. (2003); Yuanjiacun BIFs are from Hou et al. (2014); Gongchangling BIFs from Li et al. (2014); Sanjiang BIF are from Yan et al. (2010) and Xinyu BIF are from Shen et al. (2008)).
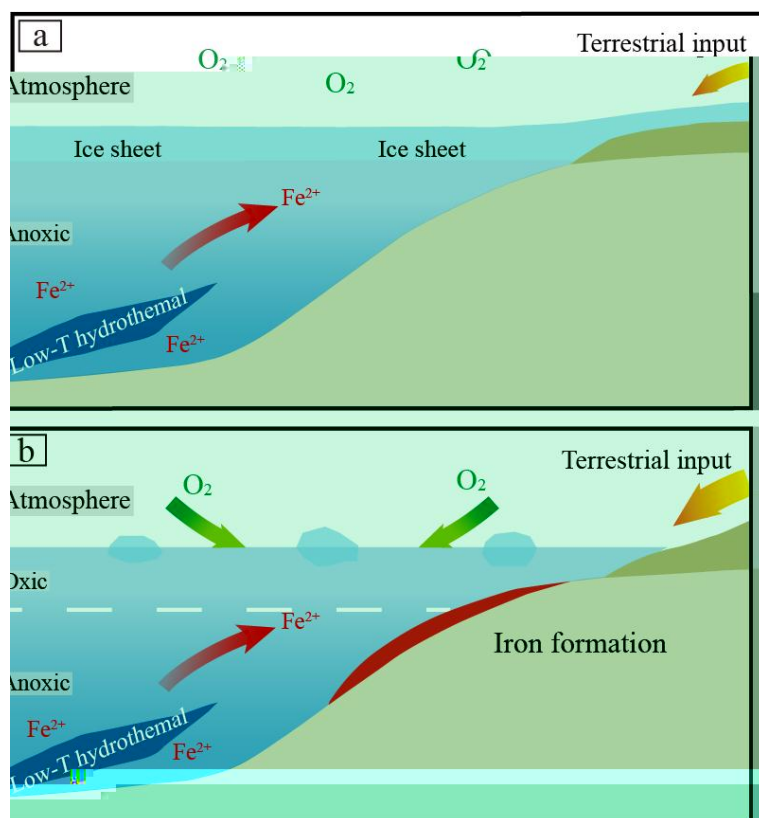
Fig. 12 Cartoon model of the formation of the Baijianshan BIF (see details in the text).

Appendix Table Captions

Appendix-Table 1 LA-ICP-MS U-Pb data for zircon from tuff in the first section of the Lapeiquan Formation

Appendix-Table 2 Geochemical compositions of the Baijianshan BIF

Appendix-Table 3 Sr-Nd isotopic data of the Baijianshan BIF

Appendix-Table 4 Fe isotopic data of the Baijianshan BIF

Supplementary Table 1 Zircon U-Pb age data of the tuff from the Baijianshan BIF

Spot	U ppm	Th ppm	Th/U	$^{206}Pb/^{238}U$ Age		$^{207}Pb/^{235}U$ Age		$^{207}Pb/^{206}Pb$		$^{207}Pb/^{235}U$		$^{206}Pb/^{238}U$	
2071-1	3079	831	0.27	1335	14	1360	21	0.0887	0.0012	2.8156	0.0427	0.2301	0.0025
2071-2	805	427	0.53	898	11	1154	20	0.1027	0.0014	2.1169	0.0369	0.1495	0.0018
2071-3	529	381	0.72	776	8	1009	18	0.0965	0.0016	1.7019	0.0307	0.1279	0.0014
2071-4	155	81	0.52	835	9	1350	22	0.1458	0.0022	2.778	0.0462	0.1382	0.0015
2071-5	184	101	0.55	751	8	1009	18	0.0999	0.0016	1.7022	0.0304	0.1236	0.0013
2071-6	297	252	0.85	1273	14								

Supplementary Table 2 Geochemical compositions of Baijianshan BIF

Sample	BJS-1	BJS-2	BJS-3	BJS-4	BJS-5	BJS-6	BJS-7	BJS-8	BJS-9	BJS-10
Major elements (%)										
Fe_2O_3	53.60	41.52	56.64	52.26	30.01	36.85	41.01	45.22	39.78	48.55
SiO_2	29.91	38.96	26.81	31.20	40.92	40.79	36.97	41.77	43.66	37.59
Al_2O_3	1.56									

TFe_2O_3	21.79	28.86	44.82	42.63	26.98	13.11	40.45	11.61	11.70	11.98
SiO_2	55.06	49.87	41.24	43.65	53.64	59.90	42.80	39.94	40.91	44.55
Al_2O_3	5.24	4.93	2.81	2.86	4.83	7.58	3.84	11.36	11.45	10.76
CaO	0.81	1.02	0.75	0.75	0.76	0.84	0.65	9.77	9.31	7.45
MgO	1.57	1.51	0.74	0.86	1.36	2.32	1.31	8.40	8.54	10.38
TiO_2	0.60	0.53	0.35	0.25	0.59	0.86	0.41	3.66	3.80	3.60
MnO	0.03	0.04	0.05	0.03	0.03	0.02	0.03	0.24	0.25	0.23
P_2O_5	0.20	0.35	0.49	0.40	0.23	0.19	0.54	0.46	0.43	0.38
K_2O	3.11	2.32	0.26	0.17	1.86	3.78	1.98	1.35	1.27	0.36
Na_2O	0.94	1.25	0.14	0.19	0.63	0.77	0.88	0.94	0.98	0.59
LOI	2.06	1.97	4.57	2.89	2.9	3.19	1.92	12.02	11.39	9.60
FeO	7.97	7.26	3.89	5.29	6.06	6.57	5.31	-	-	-
Total	99.38	99.91	100.11	99.97	99.87	99.13	100.12	99.75	100.03	99.88

Trace elements (ppm)

Cr	118	81.0	59.7	10.5	86.2	112	50.9	214	214	306
Ni	15.6	14.5	12.1	11.0	15.6	12.3	12.6	162	166	217
Co	76.1	70.2	33.7	34.7	54.0	27.1	45.3	48.0	62.9	50.7
Sc	12.2	14.4	7.97	8.11	11.7	15.1	8.11	26.4	26.1	25.7
Ba	662	562	111	19.2	359	1219	385	877	864	296
Sr	45.0	53.3	45.8	26.1	32.6	37.0	48.9	205	209	150
Rb	111	95.6	7.36	6.13	113	184	85.6	34.4	32.2	12.3
Zr	101	93.4	60.0	87.9	79.9	116	79.7	259	251	228
Hf	2.63	2.37	1.23	1.50	2.11	2.99	1.92	5.35	5.74	6.00
Ta	0.88	0.75	0.37	0.36	0.64	0.84	0.53	2.24	2.33	2.14
Ga	7.95	7.63	4.39	4.63	7.12	10.3	5.97	18.3	17.2	18.8
Cu	27.6	21.6	8.12	3.56	21.4	36.0	12.4	-	-	-
Zn	62.1	40.0	26.0	23.8	35.3	37.0	29.6	-	-	-
Pb	7.80	8.24	3.54	5.32	7.64	15.4	5.75	-	-	-
U	0.47	0.69	0.39	0.40	0.72	0.82	0.37	1.45	1.09	0.92
Th	7.26	5.14	2.81	2.97	5.52	7.11	4.11	3.32	3.37	3.18
Nb	8.35	8.21	4.19	4.86	6.80	9.50	6.11	38.0	36.5	33.6
La	26.8	20.3	13.0	9.82	19.1	22.5	17.3	36.9	34.1	33.7
Ce	58.3	44.2	30.2	22.8	42.0	46.1	39.0	77.2	72.9	74.9
Pr	7.03	5.35	3.73	2.77	5.09	5.51	4.81	9.37	9.15	9.28
Nd	29.3	22.4	16.2	11.7	21.3	22.6	20.7	37.9	36.6	40.0
Sm	6.46	4.95	3.67	2.65	4.70	4.96	4.70	8.06	8.20	9.11
Eu	1.33	1.15	0.91	0.66	1.06	1.01	1.12	1.41	1.85	2.91
Gd	6.39	5.03	4.02	3.03	4.64	4.93	5.01	7.69	7.82	8.87
Tb	1.00	0.80	0.67	0.52	0.72	0.79	0.82	1.21	1.22	1.35
Dy	5.98	4.98	4.53	3.71	4.26	4.84	5.36	6.57	7.04	7.04
Y	28.5	24.9	27.9	22.0	20.1	26.1	31.9	34.8	34.0	32.1
Ho	1.20	1.04	1.02	0.85	0.86	1.01	1.17	1.25	1.29	1.31
Er	3.23	2.94	3.00	2.59	2.33	2.82	3.38	3.11	3.15	3.20
Tm	0.45	0.43	0.46	0.40	0.34	0.41	0.50	0.39	0.40	0.39
Yb	2.87	2.93	3.06	2.76	2.20	2.69	3.36	2.28	2.36	2.28
Lu	0.43	0.45	0.49	0.45	0.33	0.41	0.53	0.34	0.32	0.32
	150.77	116.95	84.95	64.71	108.93	120.58	107.75	193.68	186.4	194.67
Y/Ho	23.75	23.94	27.35	25.76	23.29	25.84	27.26	27.84	26.36	24.50
La/La*	1.06	1.07	1.09	1.02	1.06	1.09	1.10	1.14	1.06	1.14
Ce/Ce*	0.98	0.98	0.99	1.00	0.98	0.95	0.98	0.98	0.98	1.01
Y/Y*	0.85	0.88	1.04	0.99	0.84	0.95	1.02	0.89	0.83	0.78
Pr/Pr*	1.00	1.00	0.99	0.99	1.00	1.00	0.99	0.97	0.99	0.95
Eu/Eu*	0.97	1.08	1.10	1.08	1.07	0.96	1.08	0.54	0.69	0.97
La_N/Yb_N	0.69	0.51	0.31	0.26	0.64	0.62	0.38	10.99	9.82	10.04

Supplementary Table 3 Sr-Nd isotopic data of the Baijianshan BIF

Sample	$^{87}Rb/^{86}Sr$	$^{87}Sr/^{86}Sr$		$(^{87}Sr/^{86}Sr)_i$	$^{147}Sm/^{144}Nd$	$^{143}Nd/^{144}Nd$		$T_{DM}(Ga)$	
BJS-1	0.0433	0.717927	0.000004	0.7175	0.1457	0.512425	0.000006	1.63	0.65
BJS-4	4.2608	0.727751	0.000009	0.6829	0.1308	0.512394	0.000003	1.39	1.46
BJS-5	1.4305	0.728893	0.000008	0.7138	0.1378	0.512363	0.000003	1.58	0.19
BJS-7	2.4192	0.729423	0.000009	0.7040	0.1473	0.512376	0.000002	1.78	-0.45
BJS-8	2.8555	0.718681	0.000003	0.6886	0.1238	0.512351	0.000004	1.36	1.27
BJS-10	2.6390	0.723954	0.000005	0.6962	0.1344	0.512364	0.000002	1.51	0.53
BJS-12	7.0891	0.740795	0.000007	0.6662	0.1333	0.512311	0.000003	1.59	-0.40
BJS-16	9.9936	0.746329	0.000008	0.6412	0.1334	0.512317	0.000003	1.58	-0.30
BJS-18	5.0054	0.731954	0.000008	0.6793	0.1373	0.51237	0.000004	1.56	0.38
2702H1	0.4737	0.711034	0.000009	0.7061	0.1286	0.512662	0.000003	0.88	6.90
2702H2	0.4355	0.711156	0.000009	0.7066	0.1354	0.512694	0.000006	0.89	6.88
2702H3	0.2322	0.710822	0.000012	0.7084	0.1377	0.512644	0.000005	1.02	5.69

Supplementary Table 4 Fe isotopic data of the Baijianshan BIF

Sample	$^{57}Fe_{IRMM-014}$		$^{56}Fe_{IRMM-014}$

19

BJS-2	2.10	0.09	1.46	1.46
BJS-5	1.78	0.02	1.24	1.24
BJS-7	2.76	0.09	1.89	1.89
BJS-9	2.49	0.05	1.69	1.69
BJS-12	3.05	0.04	2.17	2.17
BJS-17	2.80	0.01	1.91	1.91